

An optical design enabling lightweight and large field-of-view head-mounted microscopes

Received: 8 September 2021

Joseph R. Scherrer^{1,2}, Galen F. Lynch^{1,2}, Jie J. Zhang¹ & Michale S. Fee¹✉

Accepted: 30 January 2023

Published online: 16 March 2023

 Check for updates

Here we present a fluorescence microscope light path that enables imaging, during free behavior, of thousands of neurons in mice and hundreds of neurons in juvenile songbirds. The light path eliminates traditional illumination optics, allowing for head-mounted microscopes that have both a lower weight and a larger field of view (FOV) than previously possible. Using this light path, we designed two microscopes: one optimized for FOV (~4 mm FOV; 1.4 g), and the other optimized for weight (1.0 mm FOV; 1.0 g).

Miniature head-mounted microscopes have expanded the neuroscience toolkit by enabling *in vivo* optical measurements of neural activity in freely moving animals^{1,2}. Such recordings have been used to study the neural basis of behaviors that are difficult or impossible to recapitulate in head-fixed preparations³ such as social interaction⁴, vocalization⁵, sleep⁶ and navigation⁷. Despite the impact that head-mounted fluorescent microscopes have had in neuroscience, challenges remain in extending this approach to large populations of neurons and to small model organisms. Understanding how behavior is controlled by neural populations across brain regions requires simultaneous recording in thousands of neurons, which until now has been possible only in small animals using head-fixed preparations⁸. Performing these experiments in freely moving animals requires microscopes with a larger field of view (FOV) than existing technologies, which are limited to recording from several hundred individually resolvable neurons due to their limited FOV. At the same time, imaging in small organisms such as juvenile mice and juvenile songbirds requires devices with lower weights than existing microscopes, which are too heavy to be used in these small animals. Approaches such as computationally reconstructed imaging are a promising potential solution to FOV and weight limitations^{9,10} but have yet to be successfully applied to functional brain imaging. More incremental improvements to microscope designs have made progress decreasing device weight and increasing FOV^{11–14}, but these devices are still limited by design tradeoffs that constrain either weight or optical performance.

In this Brief Communication, we address these challenges and opportunities with an optical pathway that allows for lighter microscopes with larger FOVs than previously possible, reducing the tradeoff between weight and FOV inherent to previous designs.

Most epifluorescence microscopes couple excitation light using a dichroic filter placed between the objective lens and tube lens (Fig. 1a). The added path length due to the dichroic not only increases microscope dimensions, but also necessitates a larger tube lens to accommodate off-axis rays, making complex optical assemblies prohibitively heavy. Microscopes can be optimized for low device weight, but they typically have a limited FOV (around 1 mm²), lower resolution or decreased light-gathering ability. In contrast, our optical path brings the objective and tube lens closer together, allowing the optical assembly to be more compact without sacrificing optical performance. To do so, we eliminate the dichroic and instead introduce excitation light at the back aperture of the objective lens (Fig. 1b) with a low-profile light guide and coupling prism.

We used our light path to design two head-mounted microscopes that advance the state-of-the-art in device weight and FOV. The first design, the Featherscope, weighs 1.0 g but does not sacrifice cellular resolution across a 1.0 × 1.0 mm FOV, enabling neural recordings in animals that are too small for existing head-mounted microscopes. We used this microscope to report functional calcium imaging in freely behaving juvenile songbirds during song learning. The second design, the Kiloscope, provides cellular resolution imaging across a 4.8 × 3.6 mm FOV in a device weighing only 1.4 g, allowing us to simultaneously record from thousands of neurons in a freely behaving mouse.

The Featherscope provides cellular resolution imaging in such a lightweight and compact package by combining the optical path described above with compact gradient index (GRIN) optics for both the objective and tube lenses (Fig. 1c and Extended Data Fig. 1a–c), a lightweight focusing mechanism, and a custom high-density image sensor printed circuit board (PCB). The Kiloscope achieves a wide

¹Department of Brain and Cognitive Sciences, McGovern Institute for Brain Research, Massachusetts Institute of Technology, Cambridge, MA, USA.

²These authors contributed equally: Joseph R. Scherrer, Galen F. Lynch. ✉e-mail: fee@mit.edu

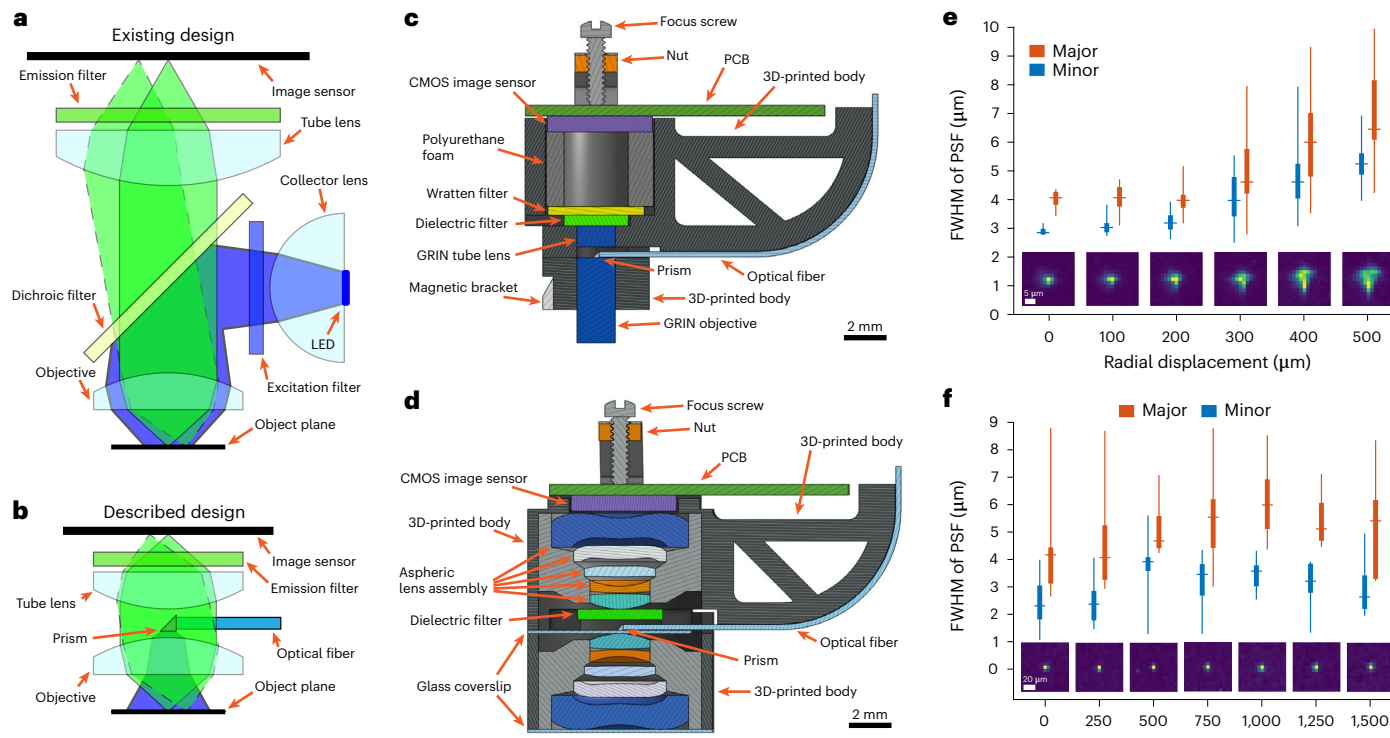


Fig. 1 | Design of head-mounted miniature microscopes. **a,b**, Schematic representation of optical path for standard head-mounted microscopes (**a**) and for the microscopes in this paper (**b**). Ray traces are the excitation light path (blue) and emission light paths for points on-axis (solid green) and off-axis (dashed green). **c**, Cross-section diagram for the Featherscope. **d**, Cross-section diagram for the Kiloscope. **e**, Measurements of the Featherscope's PSF using 1 μm

fluorescent beads ($n = 155$ beads). Orange and blue data points are measured along the major and minor axes, respectively. The horizontal line in each box represents the median, box edges are the 25th and 75th percentile, and the vertical line extends to the minimum and maximum data points. Inset images are of a representative bead at each position in the object plane. **f**, Same as **e** but for the Kiloscope ($n = 118$ beads).

FOV by using the same optical pathway in combination with precision molded plastic aspheric lens assemblies developed for smartphone cameras (Fig. 1d and Extended Data Fig. 1d). These lens assemblies achieve diffraction-limited resolution across several millimeters in a compact package. Using two such assemblies for both the objective and tube lenses in a 'double macro' configuration¹⁵, we achieve high-resolution imaging with near-flat field curvature over a large FOV (Extended Data Fig. 1e,f).

We provide illumination for both microscope designs using a fiber-coupled 473 nm laser, which allows for higher power density than an onboard light-emitting diode. The laser light is coupled into a flexible light guide that terminates at a 300 μm 90° prism mounted to the back aperture of the objective lens. The prism–fiber assembly partially occludes the optical path, reducing the overall light collection efficiency by approximately 20%. Such back-aperture occlusion has a minor effect on the diffraction limited spot size, and produces a slight increase in vignetting, but preserves the fine detail necessary for neural imaging. Additional optics placed before the input to the microscope scramble fiber modes and reduce vignetting (Extended Data Fig. 2).

Both microscope designs use a custom PCB that transmits data from a complementary metal-oxide-semiconductor (CMOS) image sensor and two analog inputs (such as electrophysiological recordings, Extended Data Fig. 3) to an interface board based on the UCLA miniscope design². For long-term recordings in behaving animals, a custom commutator transmits laser illumination light along with video data, electrophysiology data and direct current power.

We quantified imaging performance using standard resolution test targets and measurements of the point spread function (PSF). The Featherscope has a resolution of approximately 4 μm at the

center of its FOV, which decreases to 7 μm at the edges and is limited by the astigmatism of the GRIN lenses (Fig. 1e and Extended Data Fig. 1a,b). The Kiloscope has a resolution of approximately 4 μm at the center of its FOV, which decreases to about 5 μm at the edges and is limited by the sensor pixel size (Fig. 1f and Extended Data Fig. 1d,e). A higher-resolution image sensor with the same optics provides even better imaging performance (Extended Data Fig. 4). Both microscope designs have sufficiently small field curvature for typical imaging depths (Extended Data Fig. 1c,f).

To demonstrate the utility of the Featherscope in small animals, we recorded calcium activity in three freely behaving juvenile zebra finches during the subsong and protosyllable stages of song production¹⁶. Such imaging experiments were previously difficult due to the small size of these young birds, whose singing behavior is substantially impacted by implanted devices weighing more than 1.5 g. We targeted our recordings to the lateral magnocellular nucleus of the anterior nidopallium (LMAN), a brain region necessary for the earliest stages of song production¹⁶. After virally expressing GCaMP6f in LMAN, we implanted a GRIN relay lens–prism assembly at the anterior edge of LMAN and let each bird recover. We then installed the Featherscope on the bird's head and allowed the bird to freely behave for several days while recording from LMAN triggered on song (Supplementary Video 1). Implanted birds sang between 3,861 and 23,545 syllables per day, within the normal range and far exceeding the minimum amount needed for analysis of neural activity¹⁶. We analyzed the data using EXTRACT, a robust estimation algorithm for extracting microendoscopic calcium activity¹⁷, and extracted 177, 46 and 225 manually curated footprints that exhibited the spatial profile and temporal fluctuations characteristic of neuronal calcium signals in cortex¹⁸.

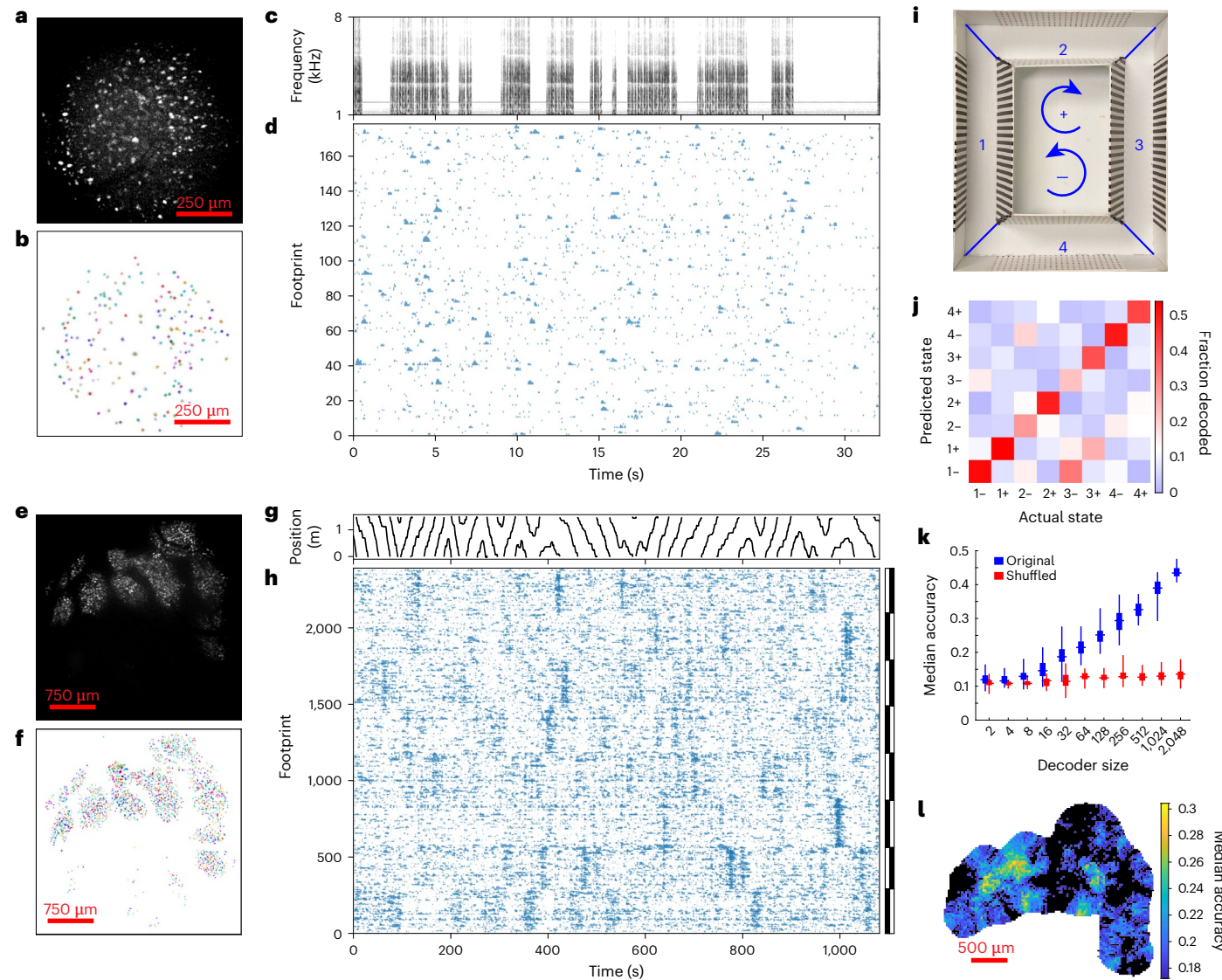


Fig. 2 | Demonstration of microscopes in awake, freely behaving animals. **a**, Maximum intensity projection of fluorescence signal from AAV9-CAG-GCaMP6f expression in the LMAN of a 49-day-old zebra finch imaged during song production. The dorsal portion of the FOV is at the top, and the medial portion is to the left. Image is representative of three birds imaged. **b**, Spatial footprints of 177 footprints extracted using EXTRACT. **c,d**, Spectrogram of a single bout of juvenile song (**c**) and corresponding calcium activity for each of the footprints in **b** (**d**). **e**, Maximum intensity projection of fluorescence signal from AAV1-syn-jGCaMP7f expression in mouse cortex imaged during exploration of a circular maze. The anterior portion of the cranial window is at the top, and the medial portion is to the right. Image is representative of four mice imaged. **f**, Spatial extents of 2,382 extracted footprints that were identified as putative neurons in the raw video. **g,h**, Linear position along track (**g**) and corresponding

calcium activity for each of the footprints in **f**, sorted by NMF component indicated by vertical bars (**h**). **i**, Diagram of circular maze used for **e–h**, with quadrants and directions labeled. **j**, Decoding matrix for a set of binary SVM models trained to predict the labels in **i** based on the neural activity in **h**. White is set at chance level. **k**, Decoding accuracies for a series of $n = 64$ decoders trained on random subsets of footprints of different sizes, using both the original data (blue) and temporally shuffled activities (red). The horizontal line in each box represents the median, box edges are the 25th and 75th percentile, and the vertical line extends to the minimum and maximum data points. **l**, Map of decoder accuracies using the 32 closest footprints less than 270 μm to a given point. Pixels that do not meet a significance threshold (Benjamini–Hochberg false discovery rate 5%) are plotted in black.

(Fig. 2a–d and Extended Data Fig. 5). The activity patterns of almost all footprints recapitulate the sparse random bursting seen in previous observations of LMAN activity during song (Fig. 2c,d)¹⁹.

To demonstrate the performance of the Kiloscope, we used the microscope to record in four freely moving mice and were able to simultaneously record more than a thousand neurons in cortex in multiple mice (Fig. 2e–h and Extended Data Fig. 6). For these experiments, we stereotactically located a region of the mouse brain at coordinates associated with primary visual and somatosensory regions, performed approximately 20 viral injections of GCaMP7f across a 4-mm-diameter region of cortex, and then implanted a 4-mm-diameter

glass window in the skull. After letting each mouse recover, we installed the Kiloscope on the head and allowed it to freely explore a circular maze (Fig. 2i) while recording calcium activity for several minutes (Supplementary Video 2). We then analyzed the data using EXTRACT and extracted 2,948, 401, 1,029 and 112 footprints in these mice. In the data from the mouse with the most footprints, manual curation using the same criteria described above yielded 2,382 footprints. Lateral shifts of the image due to mouse motion were small (root-mean-square displacement of 0.13 pixels or 0.7 μm (Extended Data Fig. 7)). These shifts were corrected using NoRMCorre²⁰ before footprint extraction.

We further analyzed the neural activity recorded by the Kiloscope in one mouse as follows. Extracted neural activity was sorted by non-negative matrix factorization (NMF) factor to highlight potential low-dimensional components (Fig. 2h). Note that the correlated activity visible in each component is driven by footprints from across the FOV (Extended Data Fig. 8). We trained a support vector machine (SVM) model on half of the data and used the other half to decode the mouse's combined position and movement direction, with the resulting accuracy at least three times chance level (Fig. 2j, $P < 0.001$, Monte Carlo sampling of $n = 1,000$ shuffled datasets). The accuracy of the decoder depended on the number of footprints used (Fig. 2k, $P \leq 2.7 \times 10^{-4}$ for all decoder sizes, Mann–Whitney U). Notably, footprints in different regions of the FOV yielded substantially different decoding accuracies (Fig. 2l). We used the same approach to decode even more fine-grained position information (Extended Data Fig. 9, $P < 0.001$, Monte Carlo sampling as in Fig. 2j). An examination of individual neural firing rate maps yielded footprints whose activity was localized to subregions of the maze (Extended Data Fig. 10).

Overall, these microscopes afford the opportunity to record populations of neurons in freely behaving animals previously inaccessible to functional imaging, and to acquire data in larger populations of neurons than previously possible with head-mounted microscopes. In recent years, important discoveries have been made using small model organisms such as food-caching birds, tree shrews, singing mice and bats^{21–24}. We anticipate that more sophisticated miniaturized open-source tools for single-neuron physiology will allow further progress using these animals. Access to datasets with thousands of neurons in freely moving animals will advance our understanding of how populations of neurons underlie natural behaviors, such as navigation and social interaction, that are difficult to study in head-fixed preparations.

Online content

Any methods, additional references, Nature Portfolio reporting summaries, source data, extended data, supplementary information, acknowledgements, peer review information; details of author contributions and competing interests; and statements of data and code availability are available at <https://doi.org/10.1038/s41592-023-01806-1>.

References

- Ghosh, K. K. et al. Miniaturized integration of a fluorescence microscope. *Nat. Methods* **8**, 871–878 (2011).
- Cai, D. J. et al. A shared neural ensemble links distinct contextual memories encoded close in time. *Nature* **534**, 115–118 (2016).
- Aghajan, Z. M. et al. Impaired spatial selectivity and intact phase precession in two-dimensional virtual reality. *Nat. Neurosci.* **18**, 121–128 (2015).
- Li, Y. et al. Neuronal representation of social information in the medial amygdala of awake behaving mice. *Cell* **171**, 1176–1190. e17 (2017).
- Roberts, T. F. et al. Identification of a motor-to-auditory pathway important for vocal learning. *Nat. Neurosci.* **20**, 978–986 (2017).
- Chen, K.-S. et al. A hypothalamic switch for REM and Non-REM sleep. *Neuron* **97**, 1168–1176.e4 (2018).
- Ziv, Y. et al. Long-term dynamics of CA1 hippocampal place codes. *Nat. Neurosci.* **16**, 264–266 (2013).
- Sofroniew, N. J., Flickinger, D., King, J. & Svoboda, K. A large field of view two-photon mesoscope with subcellular resolution for *in vivo* imaging. *eLife* **5**, e14472 (2016).
- Adams, J. K. et al. Single-frame 3D fluorescence microscopy with ultraminiature lensless FlatScope. *Sci. Adv.* **3**, e1701548 (2017).
- Xue, Y., Davison, I. G., Boas, D. A. & Tian, L. Single-shot 3D wide-field fluorescence imaging with a computational miniature mesoscope. *Sci. Adv.* **6**, eabb7508 (2020).
- Liberti, W. A. III, Perkins, L. N., Leman, D. P. & Gardner, T. J. An open source, wireless capable miniature microscope system. *J. Neural Eng.* **14**, 045001 (2017).
- de Groot, A. et al. NINscope, a versatile miniscope for multi-region circuit investigations. *eLife* **9**, e49987 (2020).
- Scott, B. B. et al. Imaging cortical dynamics in GCaMP transgenic rats with a head-mounted widefield macroscope. *Neuron* **100**, 1045–1058.e5 (2018).
- Rynes, M. L. et al. Miniaturized head-mounted microscope for whole-cortex mesoscale imaging in freely behaving mice. *Nat. Methods* **18**, 417–425 (2021).
- Switz, N. A., D'Ambrosio, M. V. & Fletcher, D. A. Low-cost mobile phone microscopy with a reversed mobile phone camera lens. *PLoS ONE* **9**, 1–7 (2014).
- Aronov, D., Andelman, A. S. & Fee, M. S. A specialized forebrain circuit for vocal babbling in the juvenile songbird. *Science* **320**, 630–634 (2008).
- Inan, H. et al. Fast and statistically robust cell extraction from large-scale neural calcium imaging datasets. Preprint at *bioRxiv* <https://doi.org/10.1101/2021.03.24.436279> (2021).
- Glas, A., Hübener, M., Bonhoeffer, T. & Goltstein, P. M. Benchmarking miniaturized microscopy against two-photon calcium imaging using single-cell orientation tuning in mouse visual cortex. *PLoS ONE* **14**, 1–18 (2019).
- Ölveczky, B. P., Andelman, A. S. & Fee, M. S. Vocal experimentation in the juvenile songbird requires a basal ganglia circuit. *PLoS Biol.* **3**, e153 (2005).
- Pnevmatikakis, E. A. & Giovannucci, A. NoRMCorre: an online algorithm for piecewise rigid motion correction of calcium imaging data. *J. Neurosci. Methods* **291**, 83–94 (2017).
- Payne, H. L., Lynch, G. F. & Aronov, D. Neural representations of space in the hippocampus of a food-caching bird. *Science* **373**, 343–348 (2021).
- Dimarco, M. M. et al. Aspects of tree shrew consolidated sleep structure resemble human sleep. *Commun. Biol.* **4**, 722 (2021).
- Okobi, D. E. Jr., Banerjee, A., Matheson, A. M. M., Phelps, S. M. & Long, M. A. Motor cortical control of vocal interaction in neotropical singing mice. *Science* **363**, 983–988 (2019).
- Finkelstein, A. et al. Three-dimensional head-direction coding in the bat brain. *Nature* **517**, 159–164 (2015).

Publisher's note Springer Nature remains neutral with regard to jurisdictional claims in published maps and institutional affiliations.

Springer Nature or its licensor (e.g. a society or other partner) holds exclusive rights to this article under a publishing agreement with the author(s) or other rightsholder(s); author self-archiving of the accepted manuscript version of this article is solely governed by the terms of such publishing agreement and applicable law.

© The Author(s), under exclusive licence to Springer Nature America, Inc. 2023

Methods

Electronics

The imaging electronics are designed around the Python 480 image sensor (ON Semiconductor NOIP1SN0480A for Featherscope and NOIP1SP0480A for Kiloscope). Our basic data acquisition (DAQ) architecture is modeled after the UCLA Miniscope system². The image sensor outputs data on a 10 bit parallel bus that is sent over coax to a DAQ board using a serializer and deserializer pair (SERDES; Texas Instruments DS90UB913A-Q1 and DS90UB913A-Q1). The DAQ board uses a Cypress CYUSB3014 controller to send the image data over a USB 3.0 bus to an acquisition computer. The DAQ board is programmed to present itself as a USB video class device (UVC) with uncompressed RGB565 video frames, as 10 bit monochrome frame formats are not supported by UVC. The 10 bit monochrome pixel data occupies the lower 10 bits of the RGB565 pixels (blue and red bits), and conversion from RGB565 to 10 bit monochrome pixel formats is done offline using custom software.

Our image sensor PCB also includes a microcontroller (Atmel ATtiny816) that is used to configure the Python 480, perform power sequencing, provide two channels of analog-to-digital conversion (ADC) and act as a bridge between the I2C bus provided by the serializer and the SPI bus on the image sensor. We use the microcontroller's onboard ADC to read two analog signals. The digitized reads are transmitted as USART serial data over the two most significant bits of the serializer's 12 bit data bus. On the DAQ side, we split the USART bus from the output of the deserializer, convert it to two low-voltage differential signal pairs, and send them off-board via an HDMI connector. We can then acquire these ADC signals with the acquisition computer using an Arduino 'Teensy' microcontroller.

The image sensor PCB was designed to be as compact and lightweight as possible. It is a six-layer PCB weighing approximately 300 mg. Because it is so small, heat management has a substantial effect on image sensor operating temperature and thermal noise. Following the NINScope system, we have disabled the image sensor PLL to reduce power consumption¹², and have attempted to maximize PCB thermal conductivity by coupling the image sensor and serializer to the ground plane using dense vias. An optional copper fin heatsink can be soldered to the PCB that weighs 150 mg and improves SNR by a factor of approximately 3. The Kiloscope data were taken with such a heatsink installed, but the Featherscope data were taken without any heatsink.

The DAQ board is a modified version of the UCLA Miniscope v3 DAQ board that uses all 12 bits of the SERDES parallel data bus, rather than the 8 in the original design. Two of the four additional bits are routed to the Cypress and used to acquire the full 10 bit output of the image sensor. The other two bits encode ADC reads and are routed to a low-voltage differential signal converter. From there, the differential signals are sent to an off-board Arduino that sends them over USB to the acquisition computer.

Optics and construction

Featherscope. The Featherscope uses all GRIN optics, which both reduces device weight and outperforms single spherical lens elements (Extended Data Fig. 1a–c). Excitation light is separated from emission light using a combination of an interference filter and an angle-independent organic dye Wratten filter. Instead of using bulky focusing mechanisms such as electrowetting lenses or screw-tightened sleeves, we provide focus adjustment by compressing the image sensor PCB against polyurethane foam using a screw bracket, allowing fine adjustment of the focus over a range of approximately 200 µm.

The Featherscope is built from microoptical components cemented into a 3D-printed body (Rosenberg Industries LLC) using UV-cure optical cement (Norland Optical Adhesive 61 and 63). The body consists of two subassemblies that are attached once the optics are installed. Body components are printed using Formlabs Black resin, known to exhibit low autofluorescence¹¹.

The lower subassembly holds the GRIN objective lens (Edmund Optics #64-537), coupling prism (Edmund Optics #66-770) and custom fiber bundle (Acrolite). Once the objective lens is installed in the body, the prism and fiber bundle are cemented to the back face and covered in a drop of black nail polish (OPI Black Onyx). The nail polish is allowed to dry, and any excess is then carefully trimmed away with a scalpel to expose as much of the back aperture of the objective as possible while maintaining enough thickness (~50 µm) to block excitation light leakage. A machined magnetic steel flange is cemented to the bottom face of the body to allow for mating with commercially available magnetic baseplates weighing 230 mg (Inscopix).

The upper subassembly holds the tube lens, optical filters, focus mechanism and image sensor PCB. The tube lens is a GRIN lens (Edmund Optics #64-537) ground down to a total length of 1.00 mm (Pioneer Precision Optics). The tube lens, dielectric filter (3 × 3 × 0.5 mm, Chroma ET525/50 m) and Wratten filter (No. 8, Knight Optical #494FWP) are attached to the body using optical cement. A foam spring is then inserted. The spring is made from compressible polyurethane foam (McMaster #86375K121) with a 3.0 mm hole punched using a biopsy punch. The image sensor board is then installed and held in place with a focus bracket. The bracket is constructed from 0.004"-thick 316 stainless steel with a #000 nut cemented to the underside using JB-Weld epoxy. A hole is punched above the nut and a #000-120 screw is threaded into the bracket. During normal operation, the screw pushes against the top of the onboard microcontroller and compresses the foam spring.

Once the two subassemblies are built, they are attached together using optical cement. The fiber bundle is then attached to the relief arm of the upper subassembly body using dental floss and potted using 5-Minute Epoxy (Loctite 1365868). Thin and flexible lines for power (Cooner Wire #CZ1174) and coaxial data (Cooner Wire #CW6563) are braided together with the fiber bundle and secured using dental floss.

Kiloscope. The Kiloscope is constructed in a similar manner to the Featherscope using two subassemblies of optics mounted in 3D-printed housings. The lower subassembly holds the objective lens, an imaging lens extracted from the rear camera module of a Samsung Galaxy S9 smartphone. These imaging lenses are carefully removed from rear camera replacement modules available from third-party vendors. The lens is installed in the printed housing and enclosed at the top and bottom by two pieces of protective No. 1 coverglass. The fiber-prism assembly is installed at the top coverglass using the same procedure as the Featherscope. The high chief ray angle of the lenses is compensated for using an image sensor with a shifted microlens array.

The upper subassembly holds the dielectric filter, tube lens, focus mechanism and imaging PCB. The tube lens is identical to the objective lens and is attached directly to the dielectric filter. Compressible sorbothane rubber strips (5000 Durometer, McMaster #8824T11) are used as focus springs and are inserted on ledges designed into the housing. The PCB is then installed and held in place with a focus bracket similar to that used with the Featherscope. The fiber is secured to the relief arm of the housing and is braided together with the electrical lines. The microscope slides into a custom machined aluminum baseplate weighing 300 mg.

The Kiloscope exhibits some degree of autofluorescence caused by the plastic optics in the objective lens assembly. However, this fluorescence bleaches out to a negligible background level after an initial exposure period.

Weight measurements for both microscopes were made by weighing each microscope with the tether attached and supported horizontally at the same height as the microscope. This method was used because the tether is permanently attached to the microscope during construction. This measurement technique thus includes a small portion (~5 cm) of the tether weight as well.

Imaging performance characterization

Optical performance modeling in Extended Data Fig. 1 was performed using Zemax OpticsStudio 19. Lens prescription data for GRIN lenses were obtained from the manufacturer. Prescription data for the aspheric lens assemblies were obtained from representative patents²⁵.

Imaging performance was measured using two methods. The first was using a standard 1951 USAF resolution test target against a fluorescent background. This method has the benefit of intuitive interpretation and broad recognizability, but it is somewhat subjective and does not include information about the resolution of the system at different points in the FOV. Miniature endoscopes such as ours have substantial aberrations that vary across the FOV and tend to be minimized at the center, so measurements using resolution test targets at a single position can overestimate the full-field resolution.

Because of these limitations, we decided to quantify the PSF of our microscopes using an array of beads imaged at various positions and vertical displacements within the FOV. The PSF contains the same information as a two-dimensional modulation transfer function measurement taken at various positions, but has the added benefit of being intuitively interpretable for researchers who are not familiar with optical engineering methods.

For the PSF data in Fig. 1, we imaged a slide of 1-μm-diameter fluorescent beads at a series of vertical positions spanning 100 μm of depth. We then found the position corresponding to the most focused image for each bead, and fit a two-dimensional Gaussian distribution to that image to find an approximate full width at half maximum (FWHM). We also measured the field curvature by plotting the vertical position of best focus as a function of radial distance (Extended Data Fig. 1). We sampled 155 and 118 beads for the Featherscope and Kiloscope analysis, respectively.

Commutator

Our commutator simultaneously provides power, radio frequency (RF) data and illumination light to our microscopes. We couple direct current power and RF data through an electrical slip ring (Moflon MSP1069) similar to existing open-source designs (University of Colorado ONE Core). We transmit light through an optical fiber threaded through the bore of the slip ring and attached to an optical rotary joint (Thorlabs RJ1) mounted coaxially with the slip ring. We drive the commutator using a motor controlled by a magnetic feedback signal, similar to existing designs²⁶.

The slip ring presents an impedance mismatch for the 50 Ohm transmission line and on its own causes disruptive signal reflections. However, because the slip ring size is a small fraction of the carrier wavelength, we can partially compensate for the mismatch by adding a small tuning capacitor (2–6 pF) in parallel with the slip ring. Using this capacitor, along with boosting the forward channel low frequency gain of the SERDES, we can transmit data through the slip ring without excessive frame dropping.

Coupling optics

The illumination coupling optics are based on a set of four aspheric lenses (Thorlabs C280TMD-A, C230TMD-A and A397-A) that adapt the laser output numerical aperture of 0.1 to the higher microscope fiber numerical aperture of 0.5. A shutter placed in between the first two lenses provides fast control over illumination to prevent photobleaching while avoiding power instability caused by modulating the laser current.

We reduce nonuniformity in the laser output using an oscillating diffuser (Optotune LSR-3005-17S-VIS) placed at the imaged laser spot between the second and third lenses. This diffuser adds a random time-varying phase to the beam waist that randomizes the fiber mode interference pattern in the object plane. The diffuser oscillates at 300 Hz, so a single frame integrates over many of these random patterns, averaging them together and reducing the overall spatial

intensity variation. As a result, changes in the bending of the fiber do not appreciably affect the pattern of illumination in the object plane. We do not observe any residual time-varying nonuniformity in the laser illumination pattern in our *in vivo* data.

The Gaussian output of the laser results in a Gaussian distribution of illumination in the object plane. This distribution combined with the optical vignetting of the microscope results in dim fluorescence signals and thus low SNR at the edges of the FOV. To compensate, we use a pair of axicons (Thorlabs AX1220) between the third and fourth lenses that transforms the Gaussian input into a relatively flat output. The precise shape of the output distribution can be adjusted by varying the distance between the axicons.

An illumination power of 200–300 μW was used to record data using the Kiloscope, which results in an average sample irradiance of 16–24 W m⁻². This illumination is comparable to that of published microscopes that use 12–55 W m⁻² to image GCaMP6f in mice¹². An illumination power of 2.0 mW was used to record in birds using the Featherscope, which corresponds to an average sample irradiance of 790 W m⁻². This value is substantially higher than the illumination needed to image in mice, but is equivalent to the power we have used with Inscopix systems in adult birds. We believe this discrepancy results from the lower level of viral expression that we can achieve in birds with viral vectors typically used in mammals.

Data analysis

In vivo imaging data were analyzed using the NoRMCorre and EXTRACT algorithms^{17,20}. For the Kiloscope data, we first ran NoRMCorre to correct for brain motion. We then ran EXTRACT using mostly default parameter values but with an increased value for the minimum cell-finding SNR of 2. For the mouse with the best calcium indicator expression, this extraction yielded 2,948 footprints, which were then manually curated by viewing the median-subtracted video in the region of each extracted footprint at times corresponding to the peak extracted activity. We scored each footprint by whether it appeared by eye to be a spatially distinct footprint modulated in time and whether it was spatially separated from blood vessels. This manual curation yielded 2,382 putative neurons and is a lower bound on the actual number of neurons in the dataset. The resulting timeseries were factored using NMF into eight component factors, and the data plotted in Fig. 2h were sorted according to these factors to highlight potential low dimensionality of the data. Activities very close to zero are not plotted for visual clarity.

For the Featherscope data, we extracted footprints using the same pipeline, with the exception that image alignment was performed using customJulia software. The extracted footprints were manually curated in the same way; for the bird with the best calcium indicator expression, this curation yielded 177 putative neurons used in the analysis. These footprints are plotted in Fig. 2d, with activities very close to zero not plotted for visual clarity.

Song production during Featherscope experiments was quantified by counting the number of syllables each bird produced each day. On many days birds sang very little because they were handled for focus adjustment or hardware modifications, so the rates cited in the paper reflect the maximum singing rate per day for each bird.

The decoding analysis in Fig. 2i–l and Extended Data Fig. 9 was carried out using a set of binary SVM classifiers in a one-versus-all encoding scheme. The model was trained using a random contiguous 50% of the data with temporal circular symmetry and tested on the other 50%. We omitted 1% of both the training and test data, at the transition between training and test data, to avoid overfitting the model on the data adjacent to the boundary. Decoding matrices were calculated by averaging the performance of many decoders on different random holdouts.

The statistical significance of the decoding matrix in Fig. 2j was determined by calculating the distribution of median decoding accuracies for a thousand decoders trained on different shuffles of the data.

Within each shuffle, each activity timeseries was circularly shifted by a different random offset sampled uniformly across possible offsets. For each decoder size bin in Fig. 2k, 64 different random subsets of footprints were used to generate corresponding decoding matrices for each subset. The median decoding accuracy reported in Fig. 2k is the median of the diagonal elements of each decoding matrix. For the maps in Fig. 2l and Extended Data Fig. 9c, decoders were trained using the 32 footprints closest to each pixel. Pixels were omitted from the analysis if there were fewer than 32 footprints within a 270 μm radius of the pixel. Pixel-wise statistical significance was determined by calculating the distribution of median decoding accuracies for a thousand decoders trained on shuffled data from 32 randomly chosen footprints.

Video processing

Example videos were generated using custom Julia software. The fluorescence signal was median filtered over time. For the mouse data video (Supplementary Video 2), the signal was temporally downsampled by a factor of 4. The image levels of both videos were adjusted for display purposes.

Maximum intensity projections (Fig. 2a,e) were calculated using custom Julia software. The fluorescence signal was first median filtered over time and then spatially bandpass filtered. The image levels of each maximum intensity projection were adjusted for display purposes.

Subjects and calcium imaging

Calcium imaging was performed in juvenile male zebra finches (*Taeniopygia guttata*) 50–70 days post-hatch (dph) during undirected song, and in 8–12-week-old C57/B6 mice during free exploration of a circular maze. Birds and mice were obtained from the Massachusetts Institute of Technology breeding facility (Cambridge, MA) and Jackson labs, respectively. Animals were housed under a 12/12 h day/night cycle at 24 °C and 35% relative humidity. Video and behavioral data were collected using custom Bonsai workflows²⁷. The care and experimental manipulation of the animals were carried out in accordance with guidelines of the National Institutes of Health and were reviewed and approved by the Massachusetts Institute of Technology Committee on Animal Care (protocols 0718-066-21 and 0520-030-23).

Before surgery, birds were isolated from their tutor at 35 dph. Birds were anesthetized with 1–2% isoflurane in oxygen and placed in a stereotaxic apparatus. LMAN was mapped using antidromic identification from the robust nucleus of the arcopallium (RA) as previously described¹⁶, and RA was injected with cholera toxin subunit B (recombinant) Alexa Fluor 647 conjugate (Invitrogen) to retrogradely label LMAN for histological verification. LMAN was then injected with AAV9.CAG.GCaMP6f.WPRE.SV40 (ref. ²⁸) (University of Pennsylvania Viral Core) using a Nanoject II (Drummond). After a period of time to allow the virus to perfuse the neural tissue, we lowered a GRIN prism relay lens (Inscopix) anterior to LMAN, and attached it to the skull using previously described methods²⁹. Ten days following the injection procedure, birds were anesthetized and a base plate (Inscopix) was attached to the skull.

Mice were anesthetized with 1–2% isoflurane in oxygen and placed in a stereotaxic apparatus. V1 was localized using stereotaxic coordinates, and a 4 mm diameter craniotomy was made to expose V1 as well as brain regions anterior and lateral to it. We then performed a series of injections of AAV1 pGP-AAV-syn-jGCaMP7f-WPRE³⁰ (Addgene) with 500–600 μm spacing across the craniotomy. We injected 200 nl of the virus per site at a depth of 200 μm below the dura. A cranial window composed of one 4-mm-diameter coverslip glued to a 5-mm-diameter coverslip (Carolina) was inserted into the craniotomy and attached to the skull. After about 2 weeks to allow for expression, a custom base plate was attached to the skull.

Reporting summary

Further information on research design is available in the Nature Portfolio Reporting Summary linked to this article.

Data availability

The imaging data used to generate the figures in this paper are freely available at the following repository: <https://academicitorrents.com/details/aa2a3d2f5ff0b3974871db47db57bc3dabf3c192>.

Code availability

The code used to perform the analysis and generate the figures in this paper is freely available under the MIT License at the following repository: <https://github.com/FeeLab/Feescope-Paper-Code>. The firmware source code along with build instructions is available under the CC BY-NC-SA 4.0 license at the following repository: <https://github.com/FeeLab/Fee-Scopes>.

References

25. Tohru, I. Imaging lens. US patent 8934179 (2015).
26. Fee, M. S. & Leonardo, A. Miniature motorized microdrive and commutator system for chronic neural recording in small animals. *J. Neurosci. Methods* **112**, 83–94 (2001).
27. Lopes, G. et al. Bonsai: an event-based framework for processing and controlling data streams. *Front. Neuroinform.* **9**, 7 (2015).
28. Chen, T.-W. et al. Ultrasensitive fluorescent proteins for imaging neuronal activity. *Nature* **499**, 295–300 (2013).
29. Okubo, T. S., Mackevicius, E. L. & Fee, M. S. In vivo recording of single-unit activity during singing in zebra finches. *Cold Spring Harb. Protoc.* **2014**, pdb.prot084624 (2014).
30. Dana, H. et al. High-performance calcium sensors for imaging activity in neuronal populations and microcompartments. *Nat. Methods* **16**, 649–657 (2019).

Acknowledgements

We thank D. Aharoni and J. Newman for many helpful discussions and for their technical expertise. In addition, we thank M. Wilson, J. Newman, J. Voigts, N. Nikbakht, A. Bahle, M. Happ, A. Tanner and J. Kornfeld for comments on the manuscript. We thank W. Guo (MIT) for providing transgenic mice and Q. Xu (MIT) for baseplate designs and for running mice. M.S.F. acknowledges funding through the McKnight Foundation. J.R.S. acknowledges funding through the Harold and Ruth Newman Family Hertz Graduate Fellowship. G.F.L. acknowledges funding through the Simons Foundation (grant 542977ASPI). J.J.Z. acknowledges funding through the NIH (R21 EY028381-01).

Author contributions

M.S.F. and J.R.S. designed the optics. G.F.L. and J.R.S. designed the circuitry. G.F.L. wrote the firmware. J.R.S. characterized optical performance. G.F.L. performed surgeries and acquired data in birds. J.J.Z. performed surgeries in mice. J.J.Z., G.F.L. and J.R.S. acquired data in mice. G.F.L. and J.R.S. processed the data. J.R.S. performed the decoding analysis. J.R.S., G.F.L. and M.S.F. wrote the paper.

Competing interests

J.R.S., G.F.L. and M.S.F. have an anticipated financial interest as part of a partnership with Open Ephys, a company working to sell open-source tools based on the technology in this paper. This project continues to be open source.

Additional information

Extended data is available for this paper at <https://doi.org/10.1038/s41592-023-01806-1>.

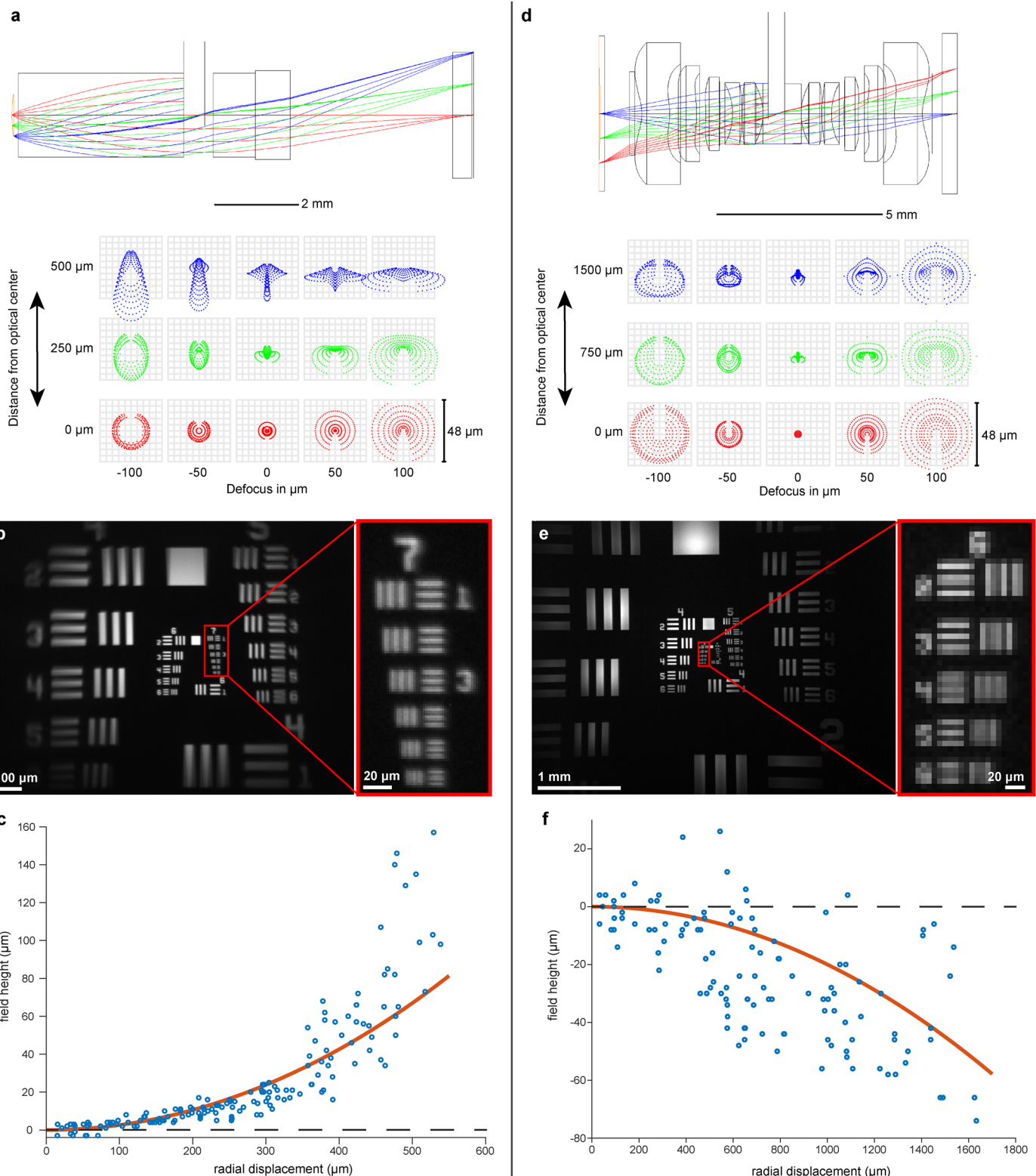
Supplementary information The online version contains supplementary material available at <https://doi.org/10.1038/s41592-023-01806-1>.

Correspondence and requests for materials should be addressed to Michale S. Fee.

Peer review information *Nature Methods* thanks Tycho Hoogland and the other, anonymous, reviewers for their contribution to the peer

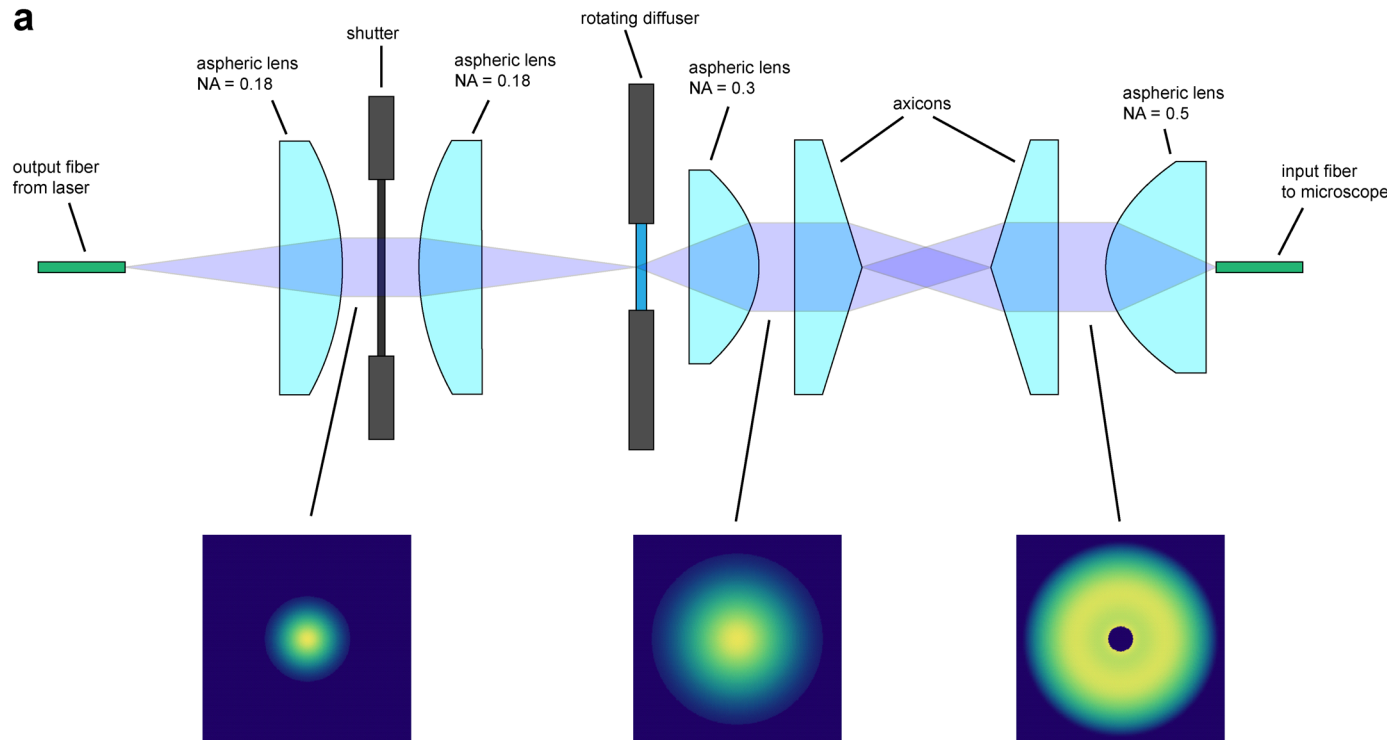
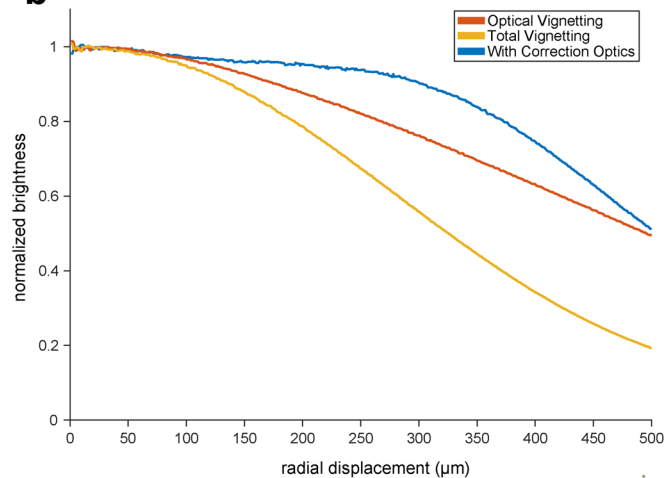
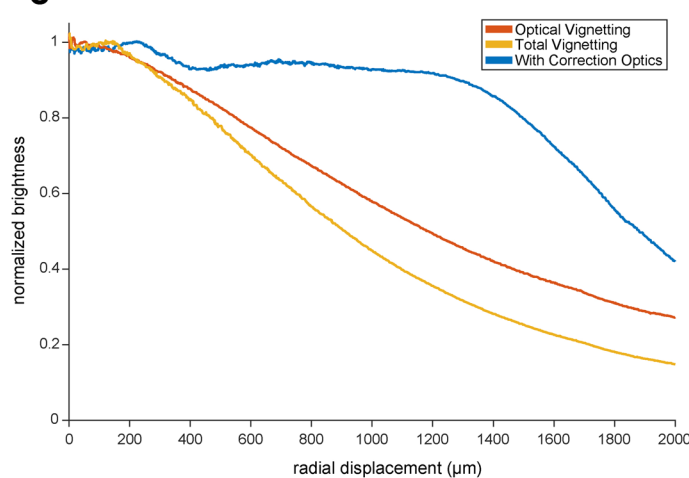
review of this work. Primary Handling editor: Nina Vogt, in collaboration with the *Nature Methods* team. Peer reviewer reports are available.

Reprints and permissions information is available at www.nature.com/reprints.



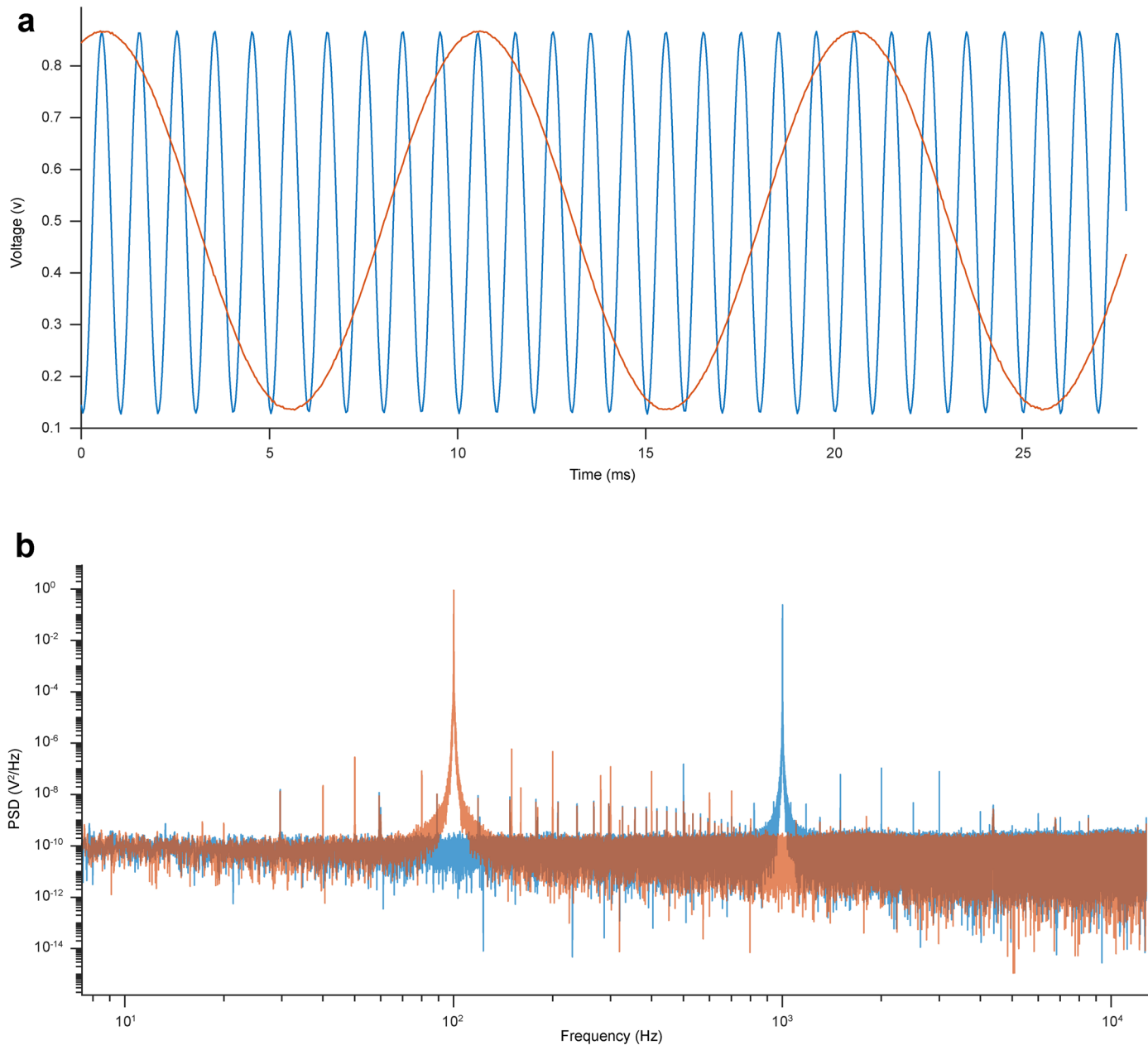
Extended Data Fig. 1 | Simulation and measurement of optical performance. **a**, Ray trace simulation of Featherscope lens assembly (above) and point spread function calculated at the image plane (below). The grid spacing is equal to the pixel width. The cross-shaped behavior of the PSF at the edges of the field of view is characteristic of astigmatic aberrations. **b**, Image taken with the Featherscope of a USAF 1951 resolution target. The line widths of the largest and smallest elements visible in the inset are $3.91 \mu\text{m}$ and $2.19 \mu\text{m}$, respectively.

c, measurements of Featherscope focal surface compared to simulations. Bead height at best focus is plotted in blue for the set of beads used in the PSF measurement in Fig. 1. Simulation results for a spherical surface of best focus is plotted in orange. **d**, Same as (a) but for the Kiloscope lens assembly. **e**, Same as in (b) but with the Kiloscope. The line widths of the largest and smallest elements visible in the inset are $6.96 \mu\text{m}$ and $4.38 \mu\text{m}$, respectively. **f**, Same as in (c) but for the Kiloscope.

a**b****c**

Extended Data Fig. 2 | Illumination coupling optics. **a**, optical assembly for adapting NA and mode scrambling the excitation light before coupling it into the microscope. The beam profile is illustrated below at various points in the assembly. Spacing between the axicons was adjusted for optimal microscope performance, and it was noted that the optimal configuration resulted in a central dark spot in the output beam. This spot is not present at the object plane due to imperfections in the fiber. **b**, Radial profile of the signal collected with the Featherscope while imaging a thin layer of fluorescent dye using different

optical configurations. Optical vignetting (orange) illustrates the effects of light losses within the microscope optics and was measured by illuminating the dye with a diffuse light source opposite the objective. Total vignetting (yellow) illustrates the decrease in fluorescent signal caused by the combination of optical vignetting and a Gaussian-shaped excitation light profile. The curve with correction optics (blue) illustrates the flat signal intensity profile that can be achieved with an axicon pair that increases the excitation intensity at the edges of the field of view. **c**, same as in **(b)** but for the Kiloscope.

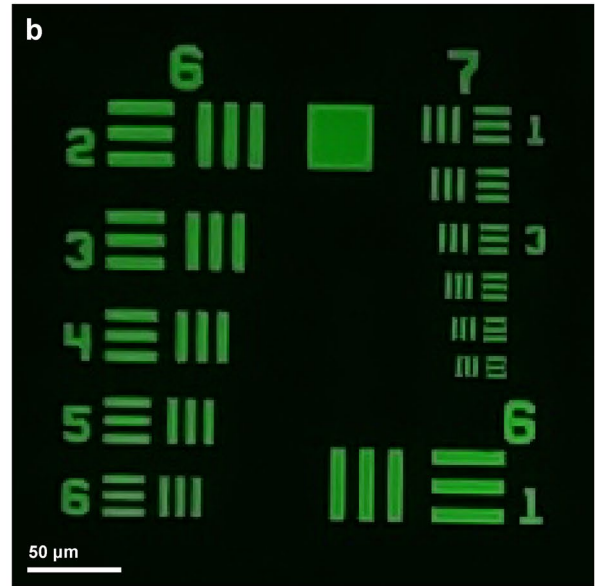


Extended Data Fig. 3 | Analog-to-digital converter functionality. **a**, Time series recording of two test signals at 100 Hz (orange) and 1000 Hz (blue) using the onboard analog-to-digital converter, sampling at 25.5 kS/s for each signal. **b**, Power spectral density of the test signals. The spectrum was calculated using

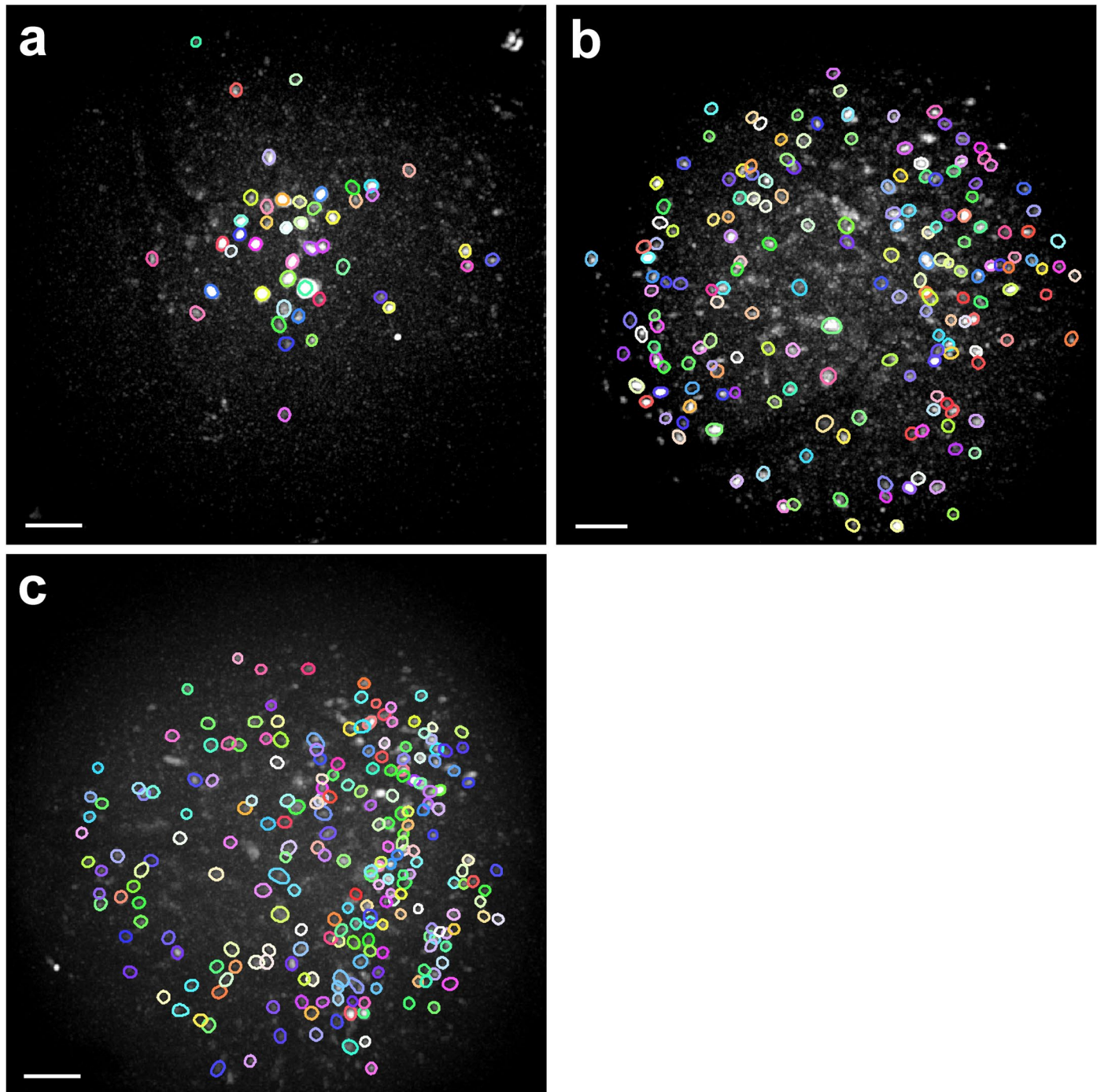
Thomson's multitaper estimate with Slepian tapers. The time series deviates from a pure tone with a root-mean-square residual of 0.2% of the full scale, calculated using the full bandwidth of the recorded signal.



Extended Data Fig. 4 | Additional performance characterization of Kiloscope optics. **a**, Image taken with the Kiloscope of a fixed coronal brain slice from one Tg(Camk2a-cre)T29-1St1 x Ai95(RCL-GCaMP6f)-D mouse. The image is corrected

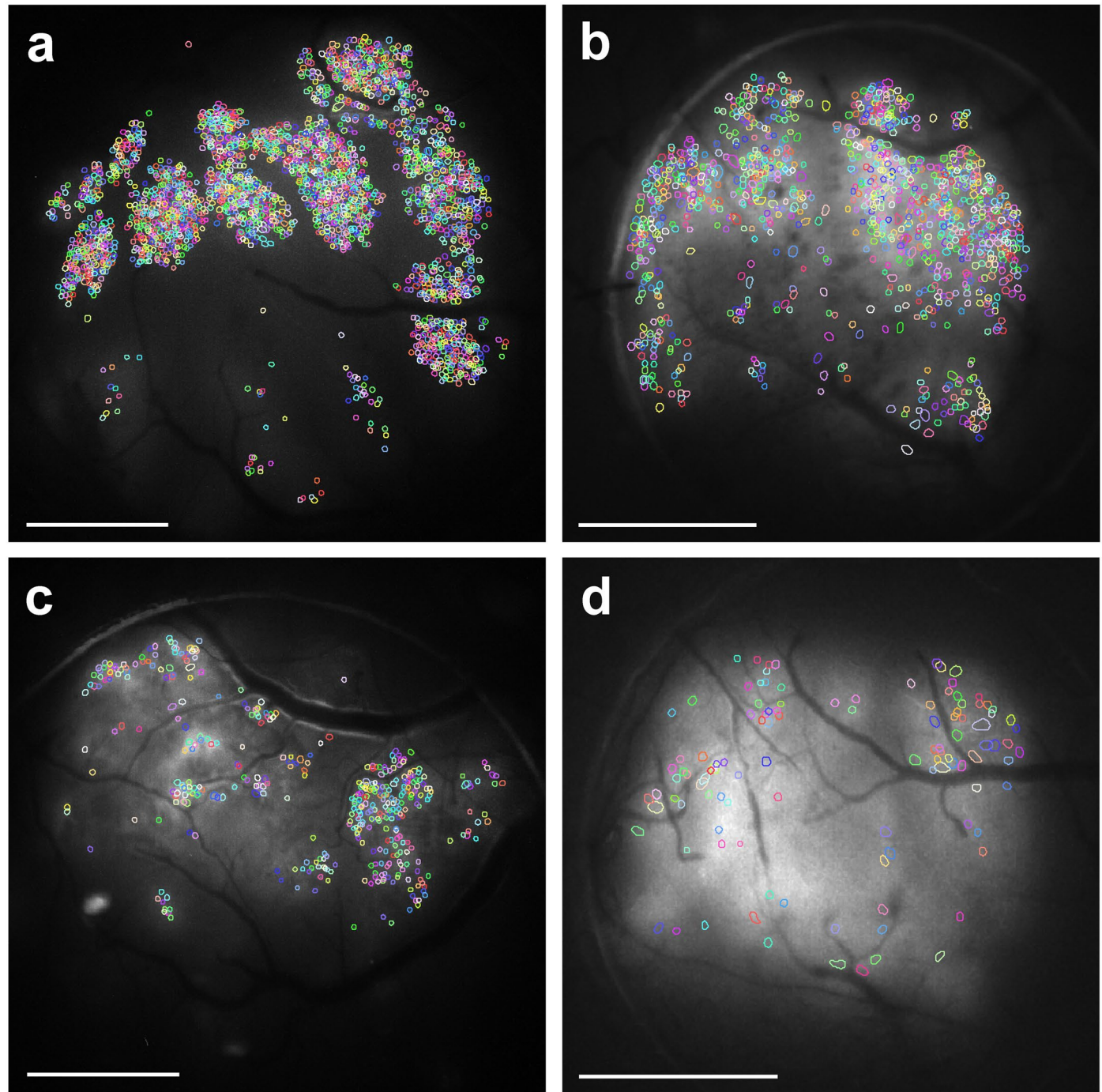


for vignetting. **b**, Image of USAF resolution target using Kiloscope optics and a Sony IMX260 image sensor with 1.4 μm pixel width. The smallest element in group 7 is resolvable and has a linewidth of 2.2 μm .



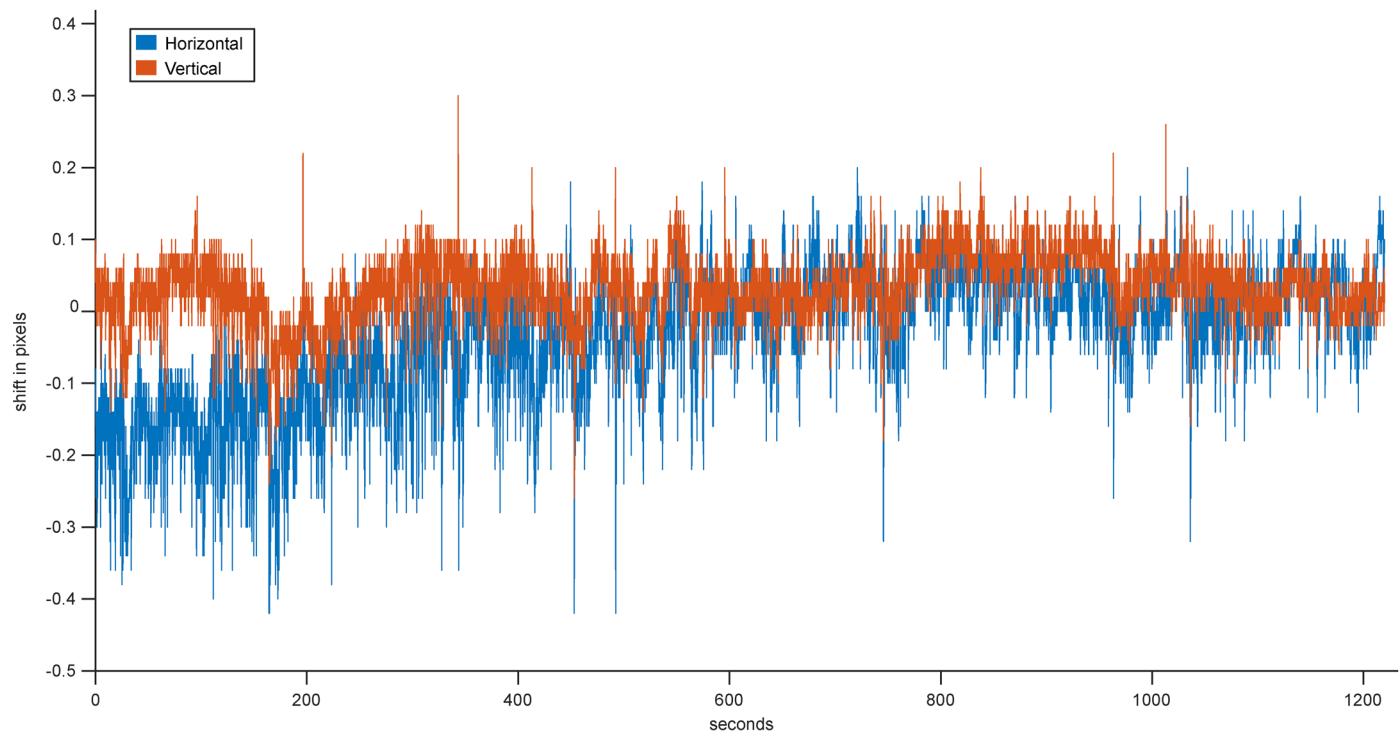
Extended Data Fig. 5 | Extraction results from the three birds presented in the paper. Footprints for each extraction are plotted as colored outlines against a grayscale background of maximum intensity of median filtered data over the course of a recording session. Footprints were extracted using EXTRACT

and manually curated based on videos of each footprint's activity. The high variability in the number of extracted footprints is likely due to variations in virus expression levels between individuals. All scale bars are 100 μm . **a**, 46 footprints after curation. **b**, 177 footprints after curation. **c**, 225 footprints after curation.

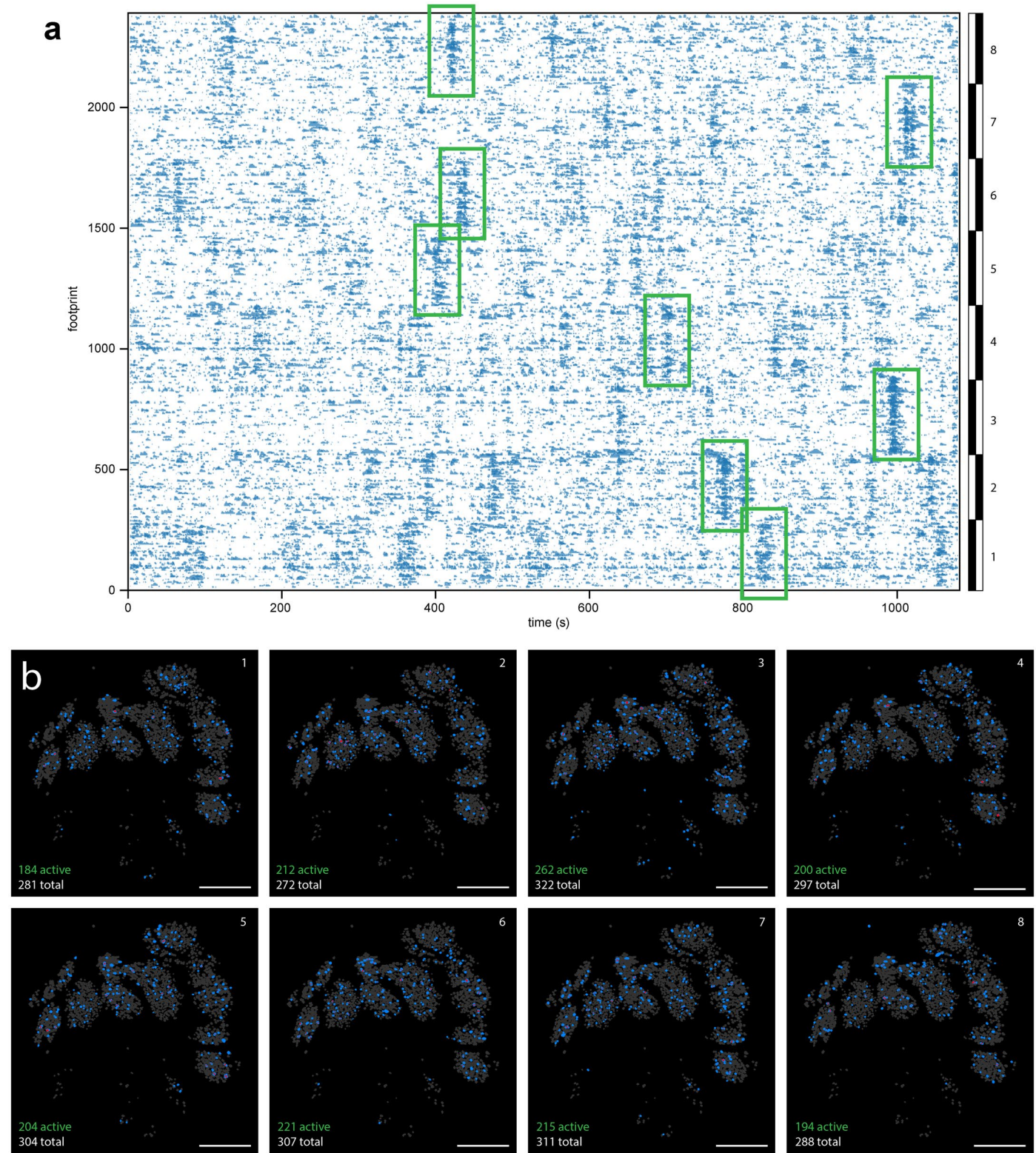


Extended Data Fig. 6 | Extraction results from the four mice presented in the paper. Footprints for each extraction are plotted as colored outlines against a grayscale background of the maximum intensity of median filtered data over the course of a recording session. Footprints were extracted using EXTRACT and manually curated for panel (a) based on videos of each footprint's activity. For panels (b–d), we inspected each footprint by eye and removed visually

anomalous footprints and footprints overlapping with blood vessels. The high variability in the number of extracted footprints is likely due to variations in virus expression levels between individuals. All scale bars are 1 mm. **a**, 4 mm cranial window, 2382 footprints after curation. **b**, 3 mm cranial window, 1029 footprints. **c**, 4 mm cranial window, 401 footprints. **d**, 3 mm cranial window, 112 footprints.

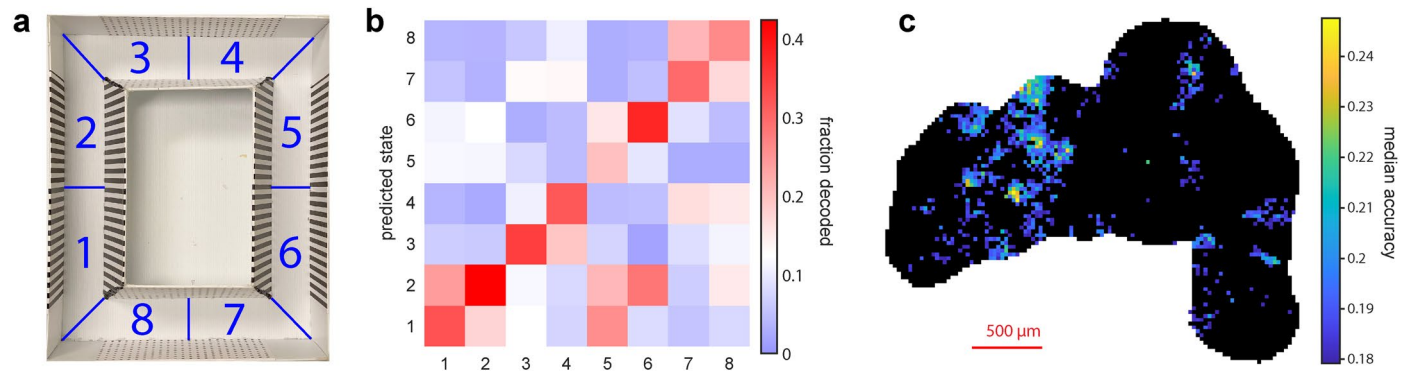


Extended Data Fig. 7 | Movement observed using the Kiloscope. Time series of horizontal and vertical displacement of the FOV, calculated using NoRMCorre, during the recording shown in Fig. 2.



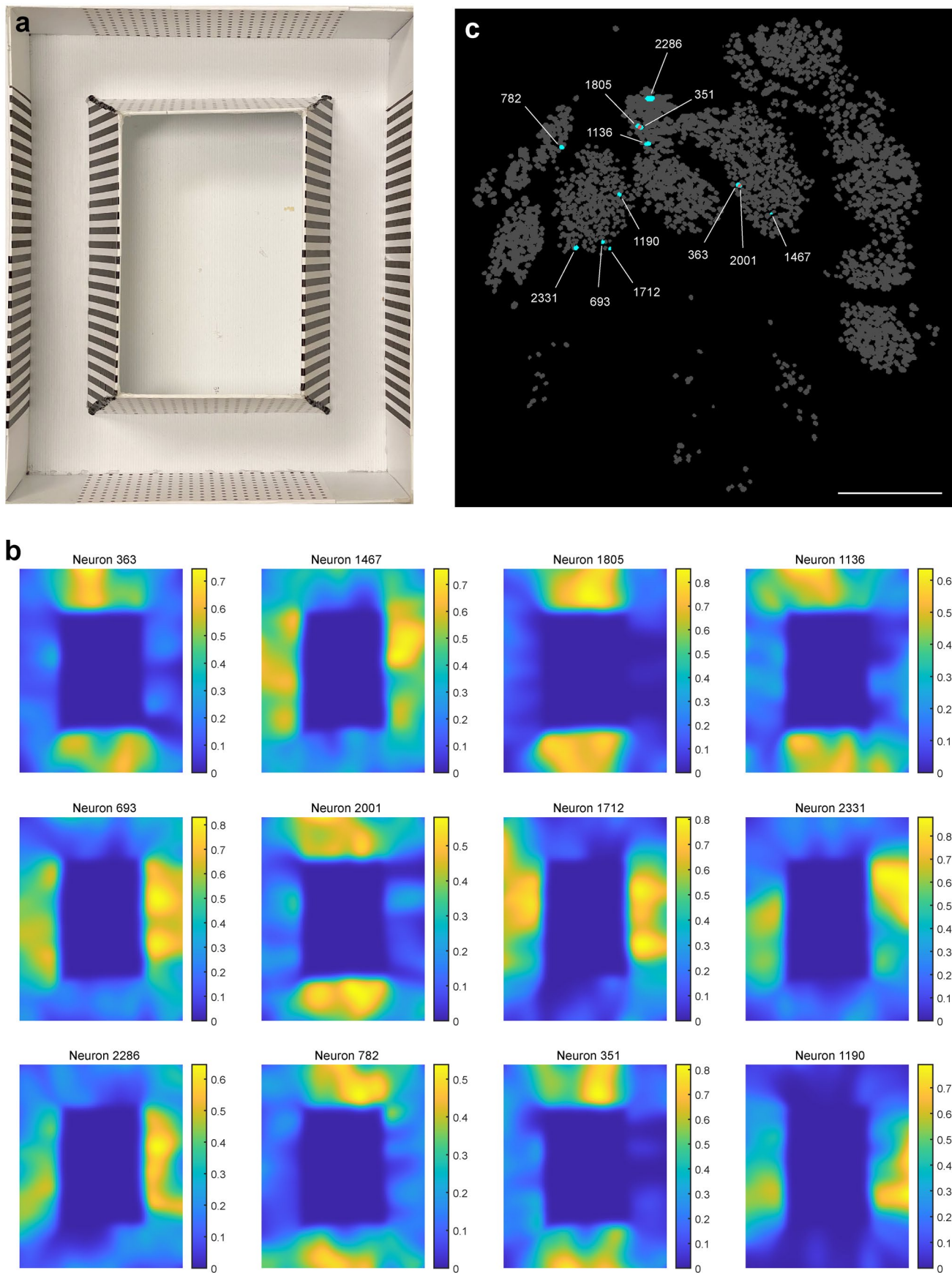
Extended Data Fig. 8 | Spatial distribution of coactive neural populations in the Kiloscope dataset shown in Figure 3. **a**, Ridgeline plot from Fig. 2d; highlighted in green is a single large correlated event for each NMF component. **b**, Locations of footprints that participate in each highlighted event. Pixels containing one active footprint are colored blue, two or more overlapping

footprints colored red, and inactive footprints colored gray. Footprints are thresholded at the 10% level. Listed in each panel are the number of footprints active in the associated event and the total number of footprints in the NMF component. All scale bars are 750 μ m.



Extended Data Fig. 9 | Decoding position within the maze with octant resolution. **a**, Circular maze with octants labeled; in this case, direction is not coded. **b**, Decoding matrix for a set of binary SVM models trained to predict the labels in (a) based on the activity in Fig. 2h. White is set at chance level. **c**, Map of

decoder accuracies using the 32 closest footprints less than 270 μm to a given point. Pixels that do not meet a significance threshold (Benjamini-Hochberg false discovery rate = 5%) are plotted in black.



Extended Data Fig. 10 | Receptive fields of selected footprints from the Kiloscope. **a**, the circular maze that the mouse explored during the recordings in Fig. 2e–h. **b**, receptive fields plotted for a collection of footprints from Fig. 2e–h. The plotted intensity is the fraction of the time a given footprint was active at a

given location. Footprints were selected by eye for large-scale structure in their receptive fields. **c**, locations of the selected footprints within the FOV. Footprints were selected blindly without knowledge of their location within the FOV. Regions of overlap between footprints are plotted in red. Scale bar is 750 μ m.

Reporting Summary

Nature Portfolio wishes to improve the reproducibility of the work that we publish. This form provides structure for consistency and transparency in reporting. For further information on Nature Portfolio policies, see our [Editorial Policies](#) and the [Editorial Policy Checklist](#).

Statistics

For all statistical analyses, confirm that the following items are present in the figure legend, table legend, main text, or Methods section.

n/a Confirmed

- The exact sample size (n) for each experimental group/condition, given as a discrete number and unit of measurement
- A statement on whether measurements were taken from distinct samples or whether the same sample was measured repeatedly
- The statistical test(s) used AND whether they are one- or two-sided
Only common tests should be described solely by name; describe more complex techniques in the Methods section.
- A description of all covariates tested
- A description of any assumptions or corrections, such as tests of normality and adjustment for multiple comparisons
- A full description of the statistical parameters including central tendency (e.g. means) or other basic estimates (e.g. regression coefficient) AND variation (e.g. standard deviation) or associated estimates of uncertainty (e.g. confidence intervals)
- For null hypothesis testing, the test statistic (e.g. F , t , r) with confidence intervals, effect sizes, degrees of freedom and P value noted
Give P values as exact values whenever suitable.
- For Bayesian analysis, information on the choice of priors and Markov chain Monte Carlo settings
- For hierarchical and complex designs, identification of the appropriate level for tests and full reporting of outcomes
- Estimates of effect sizes (e.g. Cohen's d , Pearson's r), indicating how they were calculated

Our web collection on [statistics for biologists](#) contains articles on many of the points above.

Software and code

Policy information about [availability of computer code](#)

Data collection Imaging data was acquired using custom Bonsai (v4) workflows.

Data analysis Optical ray tracing was performed using Zemax OpticsStudio v19. Neural data was analyzed using NoRMCorre, EXTRACT, custom Julia v1.6 code and custom Matlab 2020b code. Optical performance and analog-to-digital conversion performance were evaluated using custom Matlab 2020b code. Analysis code is available at <https://github.com/FeeLab/Feescope-Paper-Code>.

For manuscripts utilizing custom algorithms or software that are central to the research but not yet described in published literature, software must be made available to editors and reviewers. We strongly encourage code deposition in a community repository (e.g. GitHub). See the Nature Portfolio [guidelines for submitting code & software](#) for further information.

Data

Policy information about [availability of data](#)

All manuscripts must include a [data availability statement](#). This statement should provide the following information, where applicable:

- Accession codes, unique identifiers, or web links for publicly available datasets
- A description of any restrictions on data availability
- For clinical datasets or third party data, please ensure that the statement adheres to our [policy](#)

The imaging data used to generate the figures in this paper is freely available at the following repository: <https://academictorrents.com/details/aa2a3d2f5ff0b3974871db47db57bc3dabf3c192>

Field-specific reporting

Please select the one below that is the best fit for your research. If you are not sure, read the appropriate sections before making your selection.

Life sciences Behavioural & social sciences Ecological, evolutionary & environmental sciences

For a reference copy of the document with all sections, see nature.com/documents/nr-reporting-summary-flat.pdf

Life sciences study design

All studies must disclose on these points even when the disclosure is negative.

Sample size	A total of three birds and four mice were recorded with the microscope for the purposes of this paper. Sample sizes were chosen to demonstrate replicability while keeping the number of experimental animals to a minimum.
Data exclusions	We did not include several mice and birds that were part of early attempts to use the microscopes. These animals were excluded due to poor viral expression and intracranial bleeding.
Replication	The microscopes were tested in several animals in order to demonstrate consistent performance. Decoding results were replicated in another dataset recorded in the same animal a month earlier than that presented in the paper.
Randomization	Not relevant, no comparisons were performed across different samples or conditions.
Blinding	Not relevant, no comparisons were performed across different samples or conditions.

Reporting for specific materials, systems and methods

We require information from authors about some types of materials, experimental systems and methods used in many studies. Here, indicate whether each material, system or method listed is relevant to your study. If you are not sure if a list item applies to your research, read the appropriate section before selecting a response.

Materials & experimental systems

n/a	Involved in the study
<input checked="" type="checkbox"/>	<input type="checkbox"/> Antibodies
<input checked="" type="checkbox"/>	<input type="checkbox"/> Eukaryotic cell lines
<input checked="" type="checkbox"/>	<input type="checkbox"/> Palaeontology and archaeology
<input type="checkbox"/>	<input checked="" type="checkbox"/> Animals and other organisms
<input checked="" type="checkbox"/>	<input type="checkbox"/> Human research participants
<input checked="" type="checkbox"/>	<input type="checkbox"/> Clinical data
<input checked="" type="checkbox"/>	<input type="checkbox"/> Dual use research of concern

Methods

n/a	Involved in the study
<input checked="" type="checkbox"/>	<input type="checkbox"/> ChIP-seq
<input checked="" type="checkbox"/>	<input type="checkbox"/> Flow cytometry
<input checked="" type="checkbox"/>	<input type="checkbox"/> MRI-based neuroimaging

Animals and other organisms

Policy information about [studies involving animals](#); [ARRIVE guidelines](#) recommended for reporting animal research

Laboratory animals juvenile male wildtype zebra finch (*Taeniopygia guttata*) 50-70 days post-hatch (dph)
8-12 week old male C57/B6 mouse

Wild animals Study did not involve wild animals

Field-collected samples Study did not involve field-collected samples

Ethics oversight Massachusetts Institute of Technology Committee on Animal Care

Note that full information on the approval of the study protocol must also be provided in the manuscript.